Resonant near-surface inertial oscillations in the northeastern Gulf of Mexico

Gough, M.K.; Reniers, Ad; MacMahan, JH; Howden, SD

DOI
10.1002/2015JC011372

Publication date
2016

Document Version
Final published version

Published in
Journal Of Geophysical Research-Oceans

AGU PUBLICATIONS

JGR

Journal of Geophysical Research: Oceans

RESEARCH ARTICLE

10.1002/2015JC011372

Special Section:
Physical Processes Responsible for Material Transport in the Gulf of Mexico for Oil Spill Applications

Resonant near-surface inertial oscillations in the northeastern Gulf of Mexico

Matt K. Gough[1], A. J. H. M. Reniers[2], Jamie H. MacMahan[3], and Stephan D. Howden[4]

[1]Division of Applied Marine Physics, Rosenstiel School of Marine and Atmospheric Sciences, University of Miami, Miami, Florida, USA, [2]Delft University of Technology, Department of Hydraulic Engineering, Delft, Netherlands, [3]Department of Oceanography, Naval Postgraduate School, Monterey, California, USA, [4]Department of Marine Science, University of Southern Mississippi, Hattiesburg, Mississippi, USA

Key Points:
- Diurnal oscillations in the N.E. Gulf of Mexico are attributed to wind-forced inertial motions
- The inertial motions exhibit evidence of propagation, enhancement related to flow, and phase shifts
- Variability of the inertial oscillations provides insight into how they mix the N.E. Gulf of Mexico

Correspondence to:
M. Gough,
mgough@rsmas.miami.edu

Citation:
Gough, M. K., A. J. H. M. Reniers, J. H. MacMahan, and S. D. Howden (2016), Resonant near-surface inertial oscillations in the northeastern Gulf of Mexico, *J. Geophys. Res. Oceans*, *121*, 2163–2182, doi:10.1002/2015JC011372.

Received 5 OCT 2015
Accepted 14 MAR 2016
Accepted article online 18 MAR 2016
Published online 1 APR 2016

Abstract The inertial frequency is nearly diurnal at 30°N latitude which transects the northeastern Gulf of Mexico (NeGoM). At this latitude, near-surface inertial oscillations can amplify due to resonance with diurnal wind forcing. Diurnal oscillations have also been attributed to diurnal tidal forcing in this region. Because tidal forcing, wind forcing, and inertial oscillations are nearly diurnal, a unique series of comparative analyses are required to determine their relative influence on surface circulation. By comparing surface currents obtained by HF radar to predictions of the inertial response to wind forcing and barotropic tidal currents, it is found that diurnal oscillations in the NeGoM were predominantly due to wind-forced inertial oscillations in June 2010. The analyses provide a unique spatiotemporal perspective of inertial oscillations in the NeGoM where there is evidence of propagation, frequency and phase shifts, and amplitude variability. Because inertial oscillations mix the ocean differently than the tides, these results provide insight into how inertial oscillations potentially mixed oil from the Deepwater Horizon spill in June 2010. Near-diurnal oscillations during the winter were found to be predominantly due to tidal forcing when wind-driven inertial oscillations were diminished due to a presumably deeper mixed layer.

1. Introduction

Inertial motions are the oscillatory response of a fluid in motion due to the rotation of the Earth. They are commonly observed in the ocean as clockwise (counterclockwise) oscillatory currents in the Northern (Southern) Hemisphere superimposed on mean flow. They were originally derived by *Ekman* [1905] as the oscillatory part of the homogeneous ocean's response to wind forcing on a rotating Earth, the other part being the generation of a depth-veering current with respect to the wind direction. Inertial motions are often found to be transient because they are typically generated by strong wind shifts associated with frontal passages and exponentially decay after the winds subside [*D'Asaro*, 1985; *D'Asaro et al*., 1995; *Daddio et al*., 1978; *Pollard*, 1970; *Pollard and Millard*, 1970; *Webster*, 1968]. Inertial motions can also be generated by resonance with relatively weaker forcing at frequencies near the local inertial frequency [*Hyder et al*., 2011; *Jarosz et al*., 2007; *Simpson et al*., 2002; *Webster*, 1968; *Zhang et al*., 2009; *Zhang et al*., 2010]. The local frequency of the oscillations, $f(\phi)=2\Omega sin\phi$, is dependent on latitude, ϕ, where Ω is angular rotation of the Earth.

The critical latitudes for inertial motions are 30° north and south where the local inertial frequency is very nearly diurnal (f_d). In the vicinity of these latitudes, any near-diurnal forcing that acts upon the ocean can potentially constructively resonate with, and subsequently amplify, near-diurnal oscillations. Therefore, enhanced wind-forced diurnal inertial oscillations are readily observed near the critical latitudes [*Daddio et al*., 1978; *DiMarco et al*., 2000; *Hyder et al*., 2011; *Simpson et al*., 2002; *Zhang et al*., 2009]. This is particularly true in coastal regions where resonance with diurnal sea-breezes can occur. Additionally, diurnal sea-breezes are not just coastline localized phenomena as they have been observed up to 300 km offshore [*Simpson et al*., 2002; *Zhang et al*., 2009]. Diurnal tidal forcing can also resonate at the local inertial frequency [*Hendershott*, 1973; *Reid*, 1962; *Seim et al*., 1987].

By applying a simple model of wind-forced inertial motions that allowed the wind stress to act solely upon the surface mixed layer, the amount of energy transferred into the inertial motions was found to be

dependent on the timing of the winds, the depth of the forced homogeneous surface mixed layer, and the strength of the wind stress [*Pollard and Millard*, 1970]. The energy transferred into inertial motions was not strongly dependent on ocean depth, and surprisingly not strongly dependent on stratification or the horizontal scale of the wind stress. The most efficient transfer of wind energy occurs when the wind direction rotates with the inertial motions or when there is a sudden shift in wind direction provided that unidirectional winds are not sustained longer than half the inertial period. Realistically, not all of the wind energy is transferred into inertial motions of the mixed layer. Some energy is lost to friction, baroclinic instabilities, internal waves, and Ekman transport.

Inertial motions in the northern GoM exhibit seasonal variability where greater energy was observed in the diurnal-inertial band during the summer rather than the winter despite stronger periodic winds in the winter due to frontal passages [*DiMarco et al*., 2000; *Jarosz et al*., 2007; *Teague et al*., 2014]. This was attributed to the relatively thin mixed layer (10 m) accompanied by diurnal wind forcing in the summer as opposed to the relatively thicker layer (70 m) accompanied by intermittent atmospheric frontal wind forcing in the winter.

Because inertial oscillation amplitudes are tied to the depth of the mixed layer, spatial variability of the mixed layer due to freshwater discharge can have a profound effect on the oscillations. The NeGoM has multiple sources of freshwater discharge from inlets, rivermouths, and estuaries. The largest sources of freshwater discharge come from the Mississippi River Delta and the Mobile Bay River system. Discharge from these two sources is greater during the spring and summer compared to the fall and winter [*Morey et al*., 2002, 2003]. However, increased spatial coverage of discharge over the NeGoM was found to be due to mean northward wind forcing driving eastward Ekman transport of river discharge and not due to the amount of discharge [*Morey et al*., 2002].

Inertial oscillations are important for vertical mixing in the ocean by downward inertial wave propagation [*Kunze*, 1985], shear generation at the bottom of the mixed layer [*Zhang et al*., 2009], creation of divergent and convergent flows from spatial inertial motion variability [*Hyder et al*., 2011], and coupling with internal tidal currents [*Davies and Xing*, 2003]. The shear generated at the base of the mixed layer by diurnal wind-resonant inertial oscillations can be important for enhanced vertical mixing when moderate wind forcing is not sufficient to erode strong stratification [*Zhang et al*., 2009]. They also found that when diurnal sea-breeze-driven inertial motions were strongest, the vertical shear increased significantly, the stratification decreased, and the bulk Richardson number decreased.

The tides in the NeGoM are dominated by the K_1 and O_1 diurnal tidal constituents and exhibit a form number of $F > 6$ [*Seim et al*., 1987] with the exception of the west Florida Shelf which is dominated by the M_2 tidal constituent. The form number is the ratio of the primary diurnal to semidiurnal constituent amplitudes. Since the K_1 tides are almost at the same frequency as the inertial frequency, the K_1 tidal motions are considered to be inertial at 30°N. Tidal currents along the continental slope and DeSoto Canyon region are observed to be relatively weak, <5 cm/s [*Jarosz et al*., 2007], which is in agreement with tidal modeling efforts [*Gouillon et al*., 2010; *He and Weisberg*, 2002a; *Reid et al*., 1981]. These tidal models show that over the Mississippi Bight shelf (MBS) tidal currents amplify to approximately 10 cm/s, spatially change phase, and become more elliptical. Harmonic tidal analyses performed on observed near-surface currents over the inner MBS revealed major axis tidal current amplitudes for the K_1 (O_1) to be between 6.0 and 11.9 cm/s (5.3 and 6.7 cm/s), and both the K_1 and O_1 tidal current ellipses rotated anticyclonically [*Seim et al*., 1987]. Diurnal tidal current amplification over the shelf, where oscillations reached 20–30 cm/s, was proposed to be the result of onshore propagating Sverdrup waves due to the similar amplitude of the major and minor axes, the exhibited anticyclonic rotation, and dispersive nature of the waves [*Seim et al*., 1987]. Other causes for the diurnal tidal current amplitude increase over the region could be due to the effects of stratification [*He and Weisberg*, 2002a], the proximity to a large submarine canyon [*Carter*, 2010], and internal tides.

There have been a number of studies on inertial motions off the Louisiana-Texas coast in the western GoM [*Chen et al*., 1996; *Chen and Xie*, 1997; *Daddio et al*., 1978; *DiMarco et al*., 2000; *Zhang et al*., 2009, 2010] but there has been only one study that focused on inertial motions in the NeGoM [*Jarosz et al*., 2007]. *Jarosz et al*. [2007] observed an increase in energy offshore from the shelf break in the DeSoto Canyon region, although they did not have observations over the shelf or over deep water beyond the continental shelf. They proposed that the decrease in inertial energy at the shelf break could be due to the 30°N turning

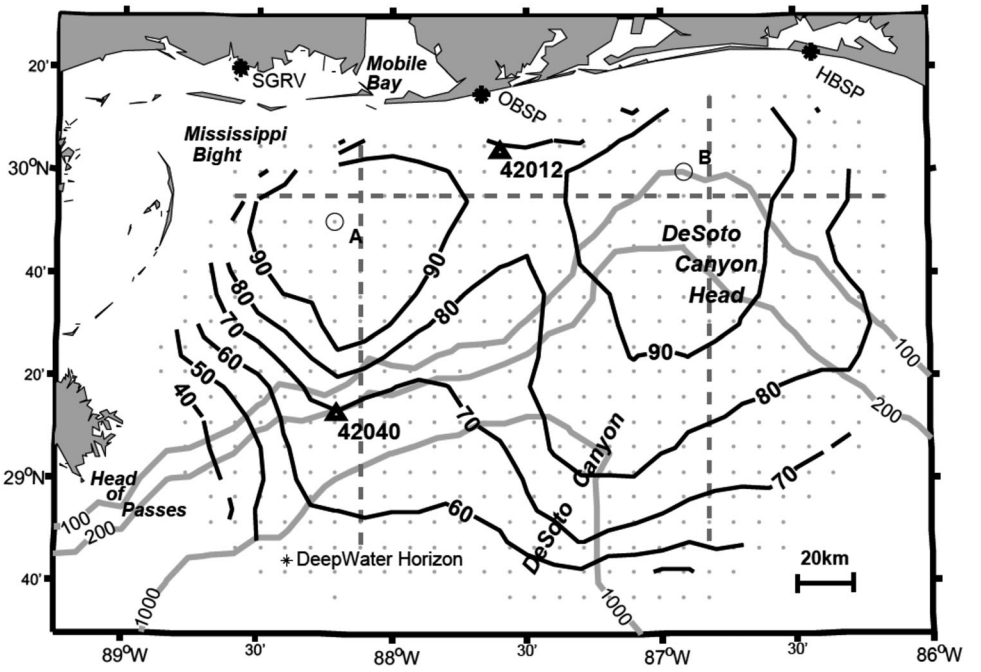

Figure 1. Northeastern Gulf of Mexico map with contours of HF radar percent coverage for June 2010. Thin gray lines represent the 100, 200, and 1000 m isobaths. Gray dots represent HF radar total vector 10 km grid data points for June 2010. Stars on coastline demark HF radar stations. Black triangles demark NDBC buoys 42012 and 42040. Gray west-east line and north-south dashed lines indicates transects for Hovmoller diagrams. Gray circles A and B indicate HF radar data points used in detailed time series analyses.

latitude for internal inertial motions and that the increase in inertial energy over the slope could be related to trapping of near-inertial energy by negative vorticity [*Hamilton et al*., 2000], offshore propagating internal waves, and/or trapping of energy by fronts. In contrast, *Chen et al*. [1996] observed a maximum of inertial current energy at the shelf break and decreases in energy both offshore and toward shore off the Louisiana-Texas coast.

The region of interest in this study is bounded by the Chandeleur Islands and Mississippi River Head of Passes to the west, the Mississippi-Alabama-Florida coastline to the north, 86.5°W to the west, and 28.5°N to the south (Figure 1). This includes the northern edge of the DeSoto Canyon and most of the DeSoto Canyon Head (DCH). The continental shelf is relatively broad off the Mississippi Bight where it extends about 100 km offshore to the 100 m isobath. The 100 m isobath then veers onshore to about 40 km offshore demarking the northern extent of the DCH. We identify the DeSoto Canyon as the region deeper than 800 m.

Here the ubiquitous strong near-diurnal resonant surface currents near the critical latitude for inertial motions (30°N) over the NeGoM are investigated with high-frequency (HF) radar measured 2-D near-surface current data obtained in June 2010. The HF radar spatial coverage spans the region between the areas investigated by *Seim et al*. [1987] who attributed diurnal oscillations to tidal currents over the inner shelf, and *Jarosz et al*. [2007] who attributed diurnal oscillations to inertial motions over the continental slope. The first goal is to determine if the diurnal oscillations observed with HF radar are due to diurnal tidal forcing or the inertial response to wind forcing. This is done by performing a series of comparative analyses between the predicted inertial response to wind forcing, predicted tidal currents, and HF radar observed currents. The inertial response to wind forcing is calculated by inputting observed wind stress into a simple "slab" model (see section 2.3). The extensive comparative analysis is necessary because tidal forcing, wind forcing, and inertial oscillations are all nearly diurnal. The near-diurnal oscillations over the MBS and DCH are shown to be predominantly due to wind-forced inertial oscillations and not due to diurnal tidal forcing. The distinction between the influence of inertial oscillations and tidal forcing is important because they vertically mix the water column differently. The second goal is to describe the near-surface spatiotemporal variability of the inertial motions which includes diurnal-inertial signal propagation, frequency shifts, and

abrupt phase changes. The spatiotemporal variability of the inertial oscillations is important for inferring how they influence mixing in the NeGoM and how they potentially mixed oil from the Deepwater Horizon spill in June 2010. Relatively smaller near-diurnal oscillations observed in January 2011, presumably due to a deeper mixed layer, are presented as a comparison to summertime conditions and are believed to be due to tidal forcing.

2. Data and Methods

2.1. HF Radar Data

Hourly horizontal (2-D) near-surface current velocities were obtained with three CODAR-type shore-based long-range (~5 MHz) HF radars (station names: HBSP, SGRV, and OBSP) maintained and operated by the University of Southern Mississippi as part of the Central Gulf of Mexico Ocean Observing System (CenGOOS). The radars cover the coastal region between the Mississippi Head, Panama City, and approximately 120 km offshore. HF radar data sets were obtained for June 2010 and January 2011. The focus is on June 2010 data which was during the Deepwater Horizon oil spill. Each radar measures near-surface current velocities toward and away the radar which are commonly referred to as "radials." In this study, the radials are processed and objectively combined using CODAR Ocean Sensor software (www.codar.com) to generate "total vectors" which are the hourly $\boldsymbol{u}$ (east-west) and $\boldsymbol{v}$ (north-south) component of near-surface current velocities interpolated onto a 9 km Cartesian grid. The total vectors are the HF radar data used herein. Two points have been selected to represent the MBS and DCH regions of interest for more detailed time series analyses (Figure 1, pts. A and B).

The fundamentals in the application of HF radar for measuring surface currents are described in numerous studies [*Barrick*, 1971, 1972; *Barrick and Lipa*, 1979; *Stewart and Joy*, 1974]. The 5 MHz HF radars measure weight-averaged currents over approximately the top 2.5 m of water. Hereafter, HF radar "near-surface" velocities are referred to as "surface" currents. HF radar measured surface velocities encompass the vector sum of the Eulerian current and the partial Stoke's drift associated with surface gravity waves less than half of the radar wavelength (or Bragg wavelength) [*Ardhuin et al*., 2009]. Studies on HF radar velocity error have found RMS differences with other types of surface current measuring instruments to range between 3 and 20 cm/s [*Chapman et al*., 1997; *Kaplan et al*., 2005; *Ohlmann et al*., 2007; *Paduan and Rosenfeld*, 1996]. HF radar error can increase in areas between two radars (baseline error) and areas far offshore due to geometric dilution of precision (GDOP) [*Chapman and Graber*, 1997]. Long-range hourly CODAR HF radar radial vector performance in a low energy environment over the west Florida shelf where the Bragg scatter echo is not strong, similar to the environment over the NeGoM, was reported to be "quite good" with RMS differences of 6–10 cm/s with near-surface ADCP data [*Liu et al*., 2010].

2.2. Wind Stress

Hourly wind velocities were obtained from NDBC buoy 42012 (measured at 5 m above sea level) and buoy 42040 (measured at 10 m above sea level) that are at 5 and 10 m above sea level, and located within the HF radar domain (Figure 1). Neutral wind stress is calculated using $\vec{\tau}=\rho C_d|w|\vec{w}$ where ρ is the density of air, C_d is the constant drag coefficient, and w is the wind speed at 10 m above sea level [*Large and Pond*, 1981]. Buoy 42012 winds are adjusted to 10 m for the neutral wind stress calculations using a log-layer correction factor. Again, the focus is on June 2010 winds during the Deepwater Horizon spill. Additional wind velocities are analyzed for May–August 2010 and January 2011.

2.3. Slab Model of Inertial Oscillation Response to Wind Forcing

The sea surface inertial current response to wind forcing is determined with a simple "slab" model following *Pollard and Millard* [1970]. This model has been applied in numerous studies and has exhibited good correlations with observed inertial oscillations [*D'Asaro*, 1985; *D'Asaro et al*., 1995; *Jarosz et al*., 2007; *Whitt and Thomas*, 2014]. The model transfers the momentum from wind stress to a vertically uniform surface layer (or "slab") that rides over a stationary layer. First, the horizontal momentum equations of the forced surface layer in the $\boldsymbol{u}$ and $\boldsymbol{v}$ direction are combined into complex form ($Z=u+iv$) and written as

$$\frac{dZ}{dt}+ifZ=\frac{T}{H}-rZ \tag{1}$$

where the wind stress is represented as $T=(\tau_x+i\tau_y)/\rho$, the local Coriolis frequency at latitude Φ is $f=2\Omega\sin\Phi$, ρ and H are the density and depth of the layer, and r is an empirically derived "decay parameter." After separating Z into an inertial oscillation contribution and mean Ekman transport velocity contribution, $Z=Z_I+Z_E$, equation (1) becomes

$$\frac{dZ_I}{dt}+\omega Z_I=-\frac{dZ_E}{dt}-\omega Z_E+\frac{T}{H} \tag{2}$$

where r and f are combined as $\omega=r+if$ and the depth of the Ekman layer is assumed to be equal to the depth of the mixed layer. The Ekman transport velocity, $Z_E=\frac{T}{\omega H}$, is known and is removed. In addition, the depth of the layer is assumed to remain constant such that $\frac{d}{dt}\left(\frac{1}{H}\right)\cong 0$. An expression for the complex inertial response due to wind forcing, Z_I, is attained by:

$$\frac{dZ_I}{dt}+\omega Z_I=-\frac{dT}{dt}\frac{1}{\omega H}\ . \tag{3}$$

Z_I can then be solved iteratively by inserting the complex form of the hourly wind stress, $T(t)$, from buoys 42012 and 42040 into the following:

$$Z_I(t+1)=Z_I(t)-dt\left[\omega Z_I(t)+\frac{T(t+1)-T(t)}{dt}\frac{1}{\omega H}\right]\ . \tag{4}$$

Hereafter, the calculated inertial response to wind stress obtained by buoy 42012 (42040) is referred to as Zi_{12} (Zi_{40}) where the subscripts 12 and 40 are the last two digits of the buoy numbers. *Zi* is used when referring to both Zi_{12} and Zi_{40}.

Typically the model is applied to the turbulent mixed layer developed by wind stress. We apply this model to a surface layer representing the lower-density semifreshwater discharge that typically extends over much of the NEGoM. Model simulations were performed with a time step of 15 min using a linear interpolation for the hourly wind stress. The damping term was set at $r=f/\pi$ which is consistent with previous work that stipulate that $r \ll f$, and that $1/r$ be between 1 and 10 days [*D'Asaro*, 1985; *Pollard and Millard*, 1970; *Whitt and Thomas*, 2014]. Using smaller time steps did not lead to significantly different results.

The depth of the surface forced layer, H, in the inertial oscillations model, is estimated to be approximately 8–10 m which is based on shipboard ADCP measurements and CTD casts obtained during the Grand Lagrangian Deployment (GLAD) in July 2012 [*Poje et al.*, 2014]. During GLAD, across-shelf shipboard ADCP transects within the HF radar domain were performed, and multiple CTD casts beyond the continental shelf and over the DeSoto Canyon were obtained (not shown). Strong ADCP echo intensity vertical gradients identify the bottom of the turbid surface layer and strong shear identifies the bottom of the mixed layer (not shown). The depth of the two types of measurements consistently agreed indicating that the depth of the turbid discharge water is the same as the depth of the mixed layer. This was corroborated with the CTD casts. Thus, the turbid discharge layer is the surface mixed layer which represents the surface forced layer in the inertial model. The 8–10 m depth is also in agreement with climatology [*Dzwonkowski and Park*, 2012], and observations from Spring and Summer 1997 [*Jarosz et al.*, 2007]. It should be noted that interannual discharge variability can affect the depth of the forced layer and inertial oscillation amplitudes [*Zhang et al.*, 2009]. A source of error in the *Zi* calculations is associated with assuming the depth of the surface layer to be constant and equivalent to the depth of the *Ekman* layer. For example, the cause of *Zi* oscillation amplitudes to be greater than observed amplitudes could be due to an underestimation of Z_E which, in turn, could be due to an underestimation of H.

2.4. Tidal Current Predictions

Barotropic tidal currents are determined using the Oregon State University Tidal Inversion Software (OTIS) (http://volkov.oce.orst.edu/tides/). Tidal current predictions show spatial amplitude and phase variability likely due to the complex coastline and bathymetry. But the complex bathymetry, particularly in the DeSoto Canyon region, brought the OTIS performance into question since a higher-resolution tidal model may be required to more accurately resolve tidal motions here. It was therefore necessary to compare OTIS

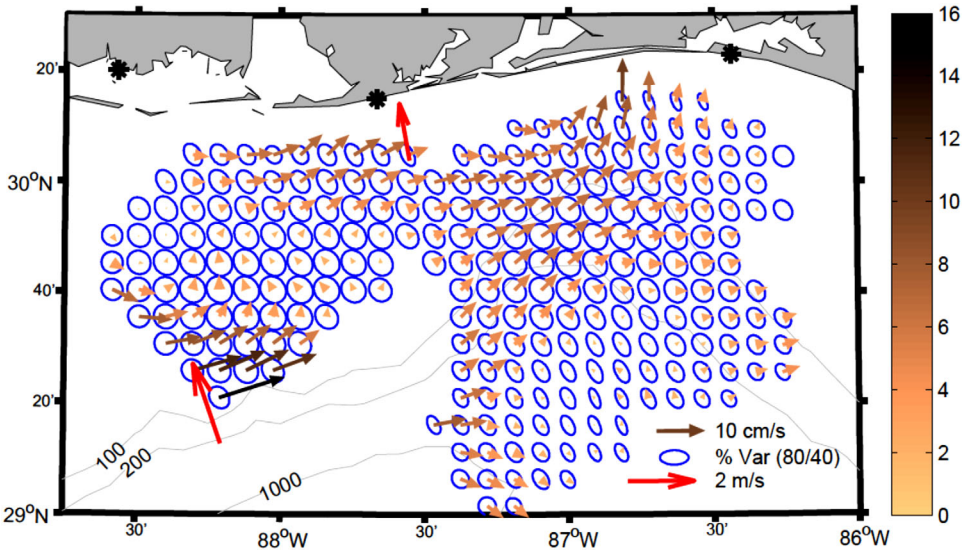

Figure 2. June 2010 HF radar measured mean flow (cm/s, size and color of arrows), mean wind speed at NDBC buoys 42012 and 42040 (m/s, red arrows), and percent of total variance in the diurnal band (0.89–1.11 cpd, blue ellipses). The ellipse in the legend indicates major (minor) axes of 80% (40%). Only coordinates with 80% HF radar temporal coverage are shown.

predictions with previous tidal model studies and nearby tidal observations. Overall, OTIS K_1 and O_1 tidal current phase and amplitude variability compare well with barotropic tidal model predictions [*Gouillon et al.*, 2010; *He and Weisberg*, 2002a; *Reid et al.*, 1981]. The tidal models, including OTIS, exhibit an amplification of the O_1 and K_1 tidal currents over MBS where their respective amplitudes are approximately 5 cm/s and at the height of the spring tidal cycle they constructively interfere to attain amplitudes of approximately 10 cm/s. Further confidence in the OTIS tidal predictions came from comparisons with tide gauge sea level heights. Sea level height observations at NDBC stations 8760922 (Pilots Station East, SW Pass), 8735180 (Dauphin Island), and 8729210 (Panama City Beach) compared surprisingly well with OTIS despite their proximity to the coastline where OTIS prediction accuracy is expected to decline. Most importantly, amplitudes compared well but there were discrepancies with the phase.

Classical harmonic tidal analysis was performed on the HF radar data but is not reported since we suspect it to be ineffective in properly separating out the diurnal tidal motions from the diurnal inertial motions in the NeGoM. The primary reason being that a much longer record length is necessary to resolve the K_1 frequency from the diurnal-inertial frequency even though the inertial frequency is not stationary. Additionally, the predicted response to wind forcing (*Zi*) frequently aligned with the predicted tidal oscillations which further corrupted harmonic analyses.

3. Observations and Results

3.1. June 2010 Mean Flow

Mean surface velocities exhibited general eastward flow, enhanced flow along the outer and inner continental shelf, and northward flow north of the DCH (Figure 2). Weaker mean flow occurred over the middle of the MBS, eastern portions of the domain, and the southeastern DCH region. In general, the HF radar velocities are in agreement with previous work on circulation in the region [*He and Weisberg*, 2002a, 2002b; *Hsueh and Golubev*, 2001; *Smith and Jacobs*, 2005; *Wang et al.*, 2003; *Weisberg et al.*, 2005; *Yuan*, 2002] although these studies generally found jet-like surface flow to exit the region toward the southeast following the 100 m isobath. Daily mean flow patterns (not shown), along with mean flow for June 2010 (Figure 2), reflect Ekman transport dynamics by exhibiting flow to the right of the wind direction. Thus, the June 2010 mean winds from the southeast enhance existing surface flow entering the domain from the southwest which follows the 50 m isobaths just inside of the edge of the continental shelf and is directed across isobaths and onshore at the northern extent of the DCH. This flow pattern is corroborated by observed June 2010 surface oil from the Deepwater Horizon spill that was transported eastward along the continental

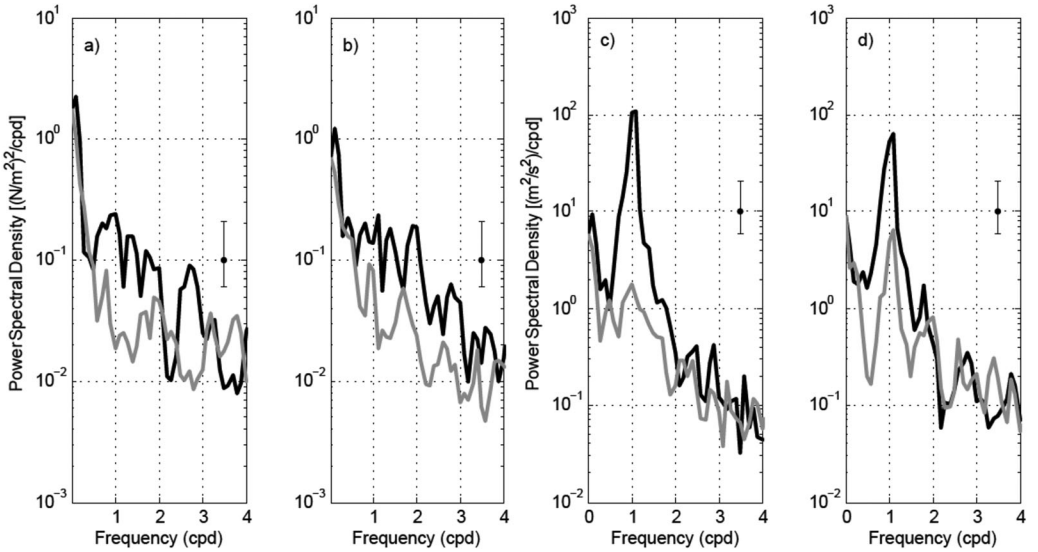

Figure 3. June 2010 Rotary spectra for wind stress at buoys (a) 42040 and (b) 42012, and surface currents at (c) pt. A and (d) pt. B. Back (gray) lines identify CW (CCW) rotation. The 95% confidence interval is provided based on 15 degrees of freedom. Data were divided into three 240 h windows. Frequency resolution is 0.096 cpd.

slope and eventually across the shelf and onto the beaches north of the DCH [*Dietrich et al*., 2012]. *Yuan* [2002] attributed cross-isobath onshore flow at the DCH to bottom-Ekman transport in response to strong along-isobath flow in combination with an offshore pressure gradient (although, in their case wind forcing was from the north and during the winter). *Huh et al*. [1981] attributed onshore flow at the DCH to intrusions of the Loop Current.

3.2. Wind Forcing

Since the inertial oscillations are hypothesized to be wind driven, the temporal phasing of wind stress is of particular importance. This is true with the phasing of wind shifts associated with atmospheric frontal passages, and the frequency of periodic wind forcing that can resonate with inertial oscillations. Additionally, the greatest resonant response to wind forcing occurs when the winds rotate along with the inertial oscillations. Rotary spectral analysis [*Gonella*, 1972] is therefore useful in studying inertial motions because it separates the CW and CCW rotational frequency spectra of a complex velocity time series. Significant spring-summer diurnal CW and CCW wind energy peaks were found over the Texas-Louisiana shelf [*DiMarco et al*., 2000] and over the DeSoto Canyon region [*Jarosz et al*., 2007] using rotary spectra. Both of these studies observed greater diurnal energy in the CW direction and less diurnal energy during winter months that corresponded with less ocean current near-diurnal energy compared to the summer.

June 2010 winds at buoys 42012 and 42040 exhibited occasional wind shifts most likely associated with atmospheric frontal passages, and brief periods of near-diurnal pulses (not shown). Rotary spectra show greater energy in the CW direction, an increase in energy toward lower frequencies, and multiple peaks between 1 and 3 cpd (Figures 3a and 3b). Even though there is not a significant diurnal peak, there is still sufficient energy across the diurnal band to excite a resonant diurnal-inertial response of the ocean. Because a significant diurnal wind energy peak was not observed in June 2010, rotary spectra was performed on wind stress from buoys 42012 and 42040 for an extended time period, May–August 2010 (not shown). These rotary spectra exhibited a significant CW peak at f_d as observed by *Jarosz et al*. [2007] indicating that diurnal wind energy was anomalously weaker than normal in June 2010.

Buoy 42040 winds, being 60 km from the Mississippi Head and 110 km from the Alabama coastline, exhibited similar diurnal energy as buoy 42012 which is only 20 km from the coastline. There was also evidence that diurnal winds can occasionally be strongest in the early morning. These observations counter the typical diurnal sea-breeze convention that winds initiate in the afternoon and are localized along the shoreline. However, it is not unprecedented for diurnal winds to be observed far offshore [*Simpson et al*., 2002; *Zhang*

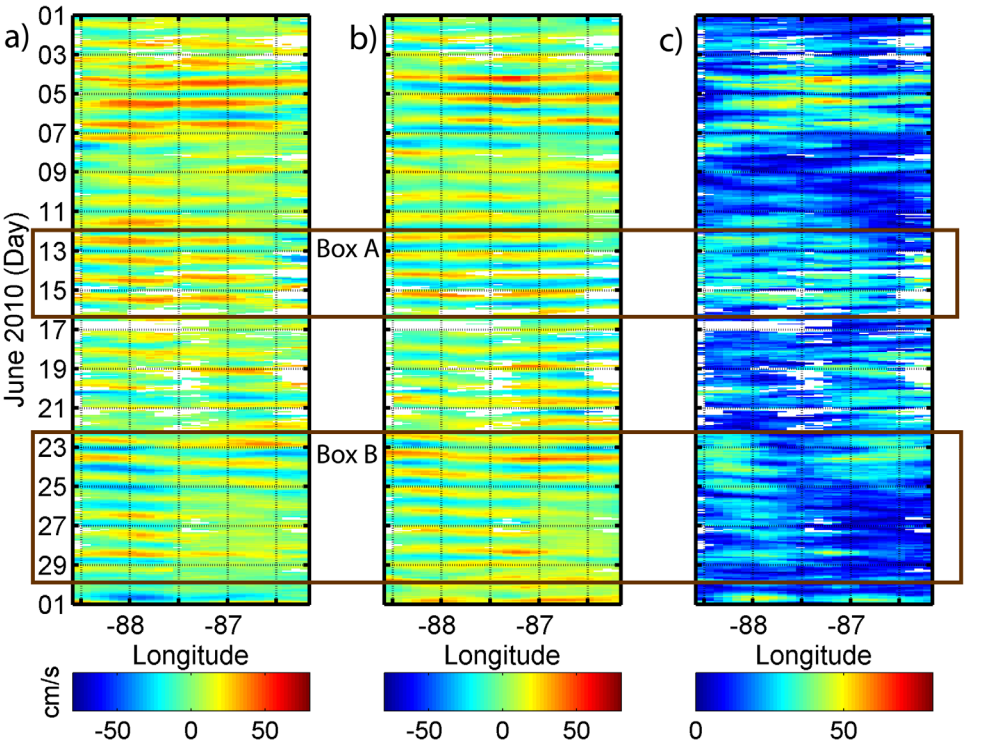

Figure 4. June 2010 surface current velocity alongshore transect (29.9°N) Hovmoller diagrams for (a) ***u*** direction and (b) ***v*** direction, and (c) magnitude.

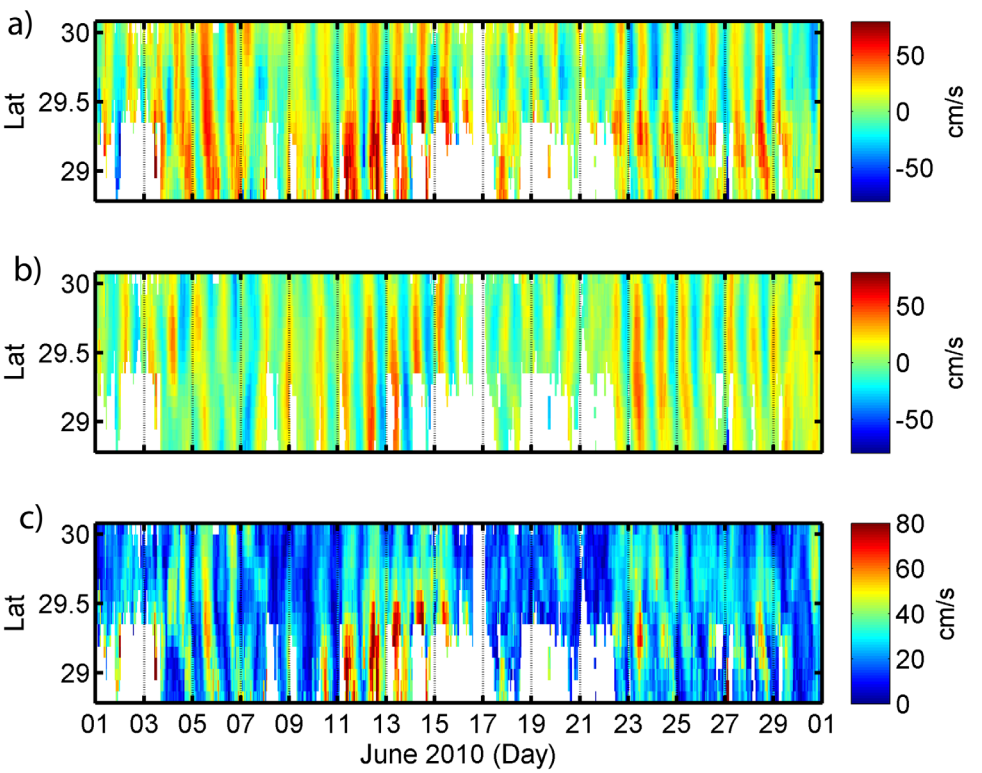

Figure 5. June 2010 surface current velocity MBS cross-shore transect (88.1°W) Hovmoller diagram for (a) ***u*** direction and (b) ***v*** direction, and (c) magnitude.

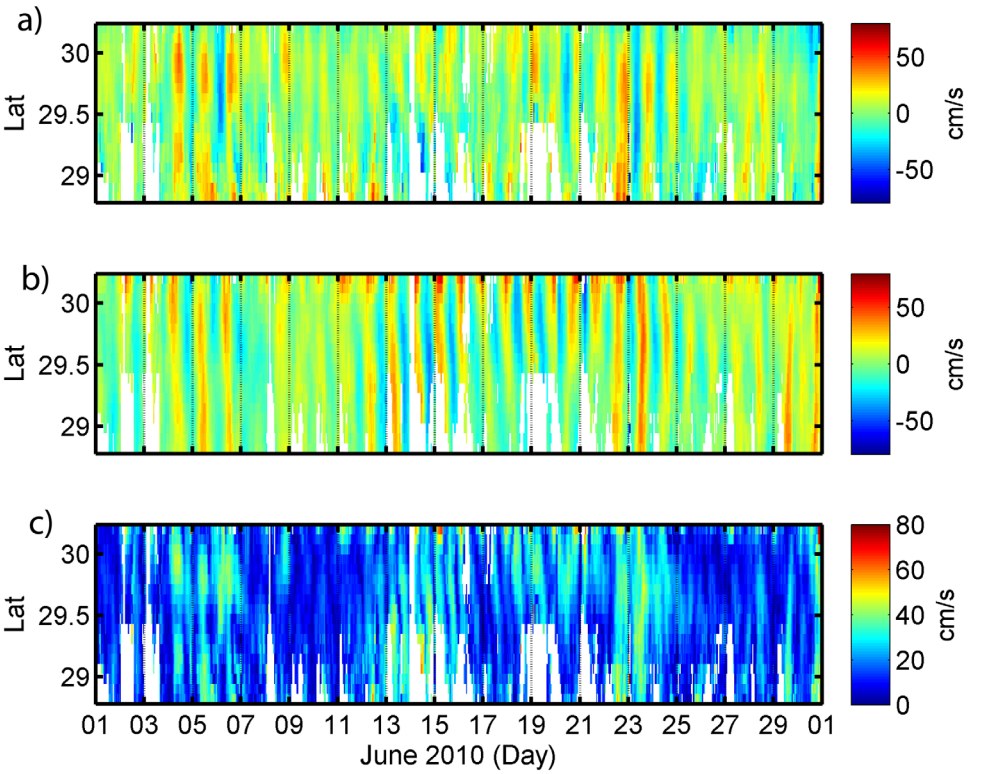

Figure 6. June 2010 surface current velocity DCH cross-shore transect (86.8°W) Hovmoller diagram for (a) ***u*** direction and (b) ***v*** direction, and (c) is the surface current magnitude.

et al., 2009], and that diurnal sea-breeze timing be out of phase with convention south of 30°N in the Northern Hemisphere [*Rotunno*, 1983; *Yan and Anthes*, 1987; *Zhang et al*., 2009].

3.3. HF Radar Observed Diurnal Surface Current Oscillations

As observed by *Jarosz et al*. [2007], large diurnal-inertial oscillations are expected in the NeGoM due to diurnal wind-forced resonance at the local inertial frequency. A good indicator of inertial oscillations in the NeGoM would be large-amplitude, spatially coherent CW-rotating near-diurnal motions. June 2010 surface currents were dominated by near-diurnal oscillations as diurnal band (0.89–1.11 cpd) variance accounted for at least 75% of the total variance over much of the domain (Figure 2). Oscillation amplitudes typically ranged between 20 and 40 cm/s and notably large oscillations reached amplitudes of approximately 45–65 cm/s over the MBS on 4–5 June (Figures 4 and 5) and 70 cm/s at the southern edge of the MBS on 11–16 June (Figure 5c). Over the DCH region north of 30°N, the ***v*** component of the oscillations exhibited large amplitudes of approximately 50 cm/s during the middle of the month (Figure 6). Overall, mean flow was much smaller than the observed oscillations and ranged between 0 and 20 cm/s (Figure 2). The oscillations predominantly rotated clockwise which is exemplified by the CW diurnal peak in rotary spectra at points A and B (Figures 3c and 3d). The DCH exhibited significant diurnal energy peaks in the both the CW and CCW directions although the CCW peak is an order of magnitude smaller (Figure 3d).

Because the oscillations are nearly diurnal and dominate the circulation in the NeGoM, percent of total variance ellipses in the diurnal band reflect the general shape of the oscillations. Following this reasoning, since Poincaré waves exhibit vector ellipses of major/minor axis ratio ω/f, frequency band variance ellipses can reflect the orientation of Poincaré waves as long as ω and f are within the frequency band. Likewise, circular variance ellipses can be used to identify and describe purely inertial motions. Variance ellipses were mostly circular indicating that the CW rotating current vectors were of equal magnitude in all directions (Figure 2). Exceptions occurred over the inner shelf, particularly north of the DCH, where variance ellipses were elongated north-south, and the eastern region of the DeSoto Canyon where diurnal band variance

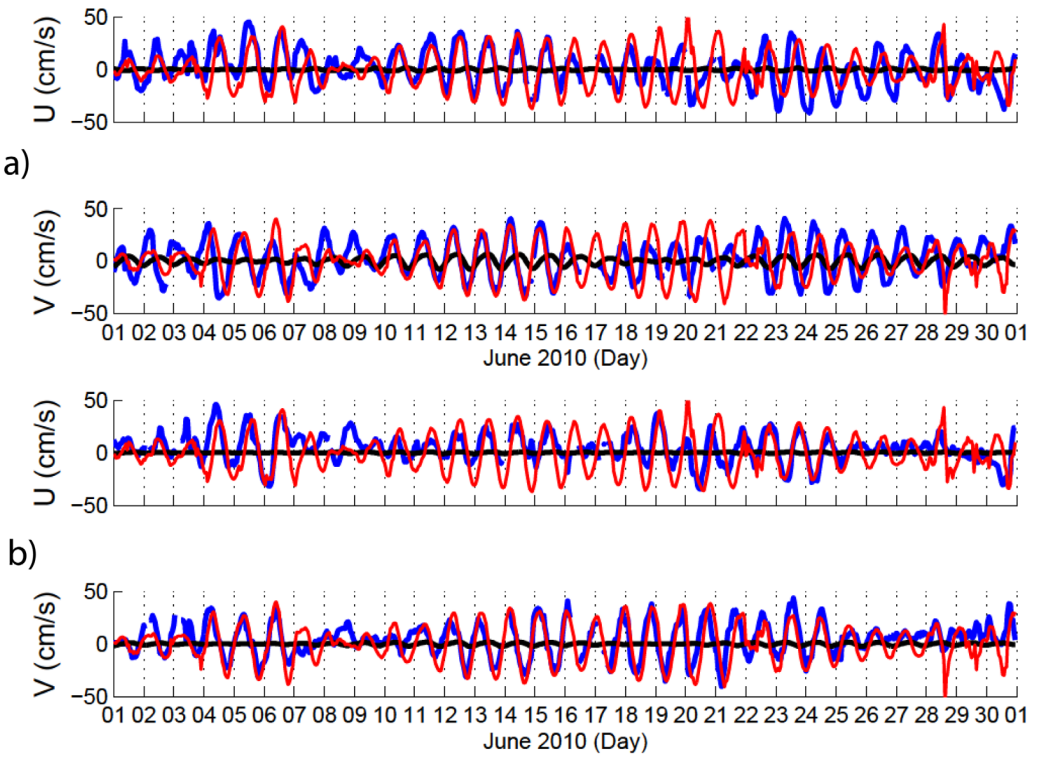

Figure 7. Pt. (a) A and (b) B June 2010 time series of Zi_{12} (red lines), HF radar measured surface currents (blue lines), OTIS tidal prediction (black lines), for (top) ***u*** and (bottom) ***v***.

decreased and ellipses were slightly elongated. The relatively greater cross-shore variance, compared to alongshore variance, along the inner shelf is influenced by periods of time when ***u*** direction oscillations were suppressed rather than a persistent suppression of ***u*** direction oscillations (Figure 7b). Over the middle of the MBS the circulation is uniquely dominated by CW rotating diurnal oscillations as mean flow was small while variance ellipses were circular and large.

Hövmöller diagrams are useful in identifying oscillatory signal propagation and abrupt spatiotemporal shifts. Considerable spatiotemporal variability in the diurnal oscillations can easily be observed the Hövmöller diagrams (Figures 4–6). We therefore focus on the most notable characteristics. With a few exceptions, there is a general offshore propagation of the diurnal oscillations between 11 and 20 June (Figure 6). The MBS and DCH regions oscillated asynchronously on 13–15 June when the MBS oscillations in the ***u*** direction lagged behind the DCH region (box A, Figure 4a), and on 24–27 June when MBS oscillations led the DCH region (box B, Figure 4). The abrupt phase differences at the interface between the regions of asynchronous oscillations are delineated by approximately 87.5°W longitude.

3.4. Point-Wise Comparisons Between Slab Model Oscillations (*Zi*) and HF Radar Surface Currents

Comparisons between *Zi* and observed oscillations at pts. A and B (Figures 7 and 8) are used to determine whether the diurnal oscillations are a response to wind forcing and gain insight into the performance of the slab model. Overall, Zi_{12} oscillations better represent the surface currents over the entire domain than Zi_{40} oscillations as linear regression results comparing HF radar currents at pts. A and B with Zi_{12} produced R^2 values between 0.24 and 0.60, and slopes ranged between 0.50 and 0.90 (Tables 1 and 2). The best fit with Zi_{12} occurred at pt. B in the ***v*** direction and the best fit with Zi_{40} occurred at pt. A in the ***v*** direction. The linear regression results may seem poor despite the apparent similarities that can be observed between observed currents and *Zi* in Figures 7 and 8, but it is important to consider that linear regression analysis is sensitive to small phase differences when comparing oscillatory signals. In addition, since pt. A is between buoys 42040 and 42012, there are times when Zi_{40} best represents the oscillations over the MBS, and times when Zi_{12} best represent the oscillations over the MBS which is another reason why the HF radar surface

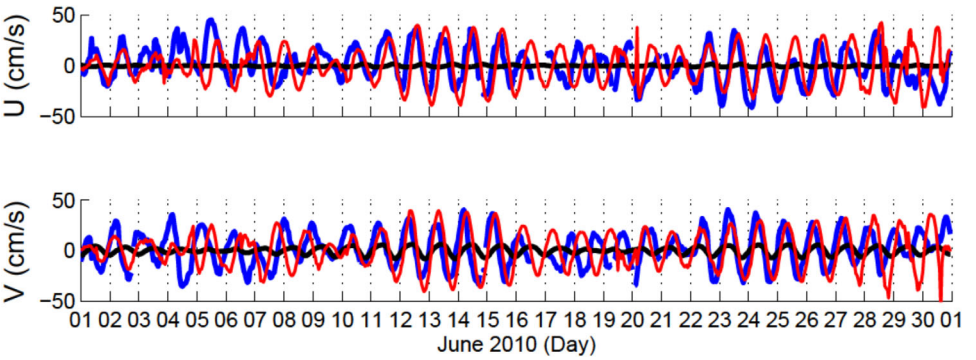

Figure 8. Pt. A June 2010 time series of Zi_{40} (red lines), HF radar measured surface currents (blue lines), OTIS tidal prediction (black lines), for (top) ***u*** and (bottom) ***v***.

current linear regression slopes decreased at point A with Zi_{12} and Zi_{40}. Running linear regression analyses (performed on overlapping 3 day sections of data every 1.5 days) between *Zi* and HF radar currents at pt. A show that at the beginning of the month, linear fits were better with Zi_{12} (Figures 9a and 9b) compared to Zi_{40} (Figures 10a and 10b), based on R^2 values and slopes. Near the end of the month, linear fits with Zi_{40} were better than those observed with Zi_{12}. Over the middle of the month linear fits were good with both Zi_{12} and Zi_{40}, and at the very end of the month, linear fits decreased with both Zi_{12} and Zi_{40} which was most likely due to strong wind shifts causing the *Zi* calculations to misrepresent the ocean response to wind forcing.

3.5. Synoptic Slab Model Oscillations (*Zi*) and HF Radar Surface Currents Comparison

Spatial cross-correlation analysis provides insight into where and when correlations and time lags occur between *Zi* and observed near-diurnal surface current oscillations. Spatial variability of the time lags can also indicate propagation or spatial frequency variability of near-diurnal oscillations. June 2010 spatial normalized cross correlations between Zi_{12} and HF radar surface currents ranged between 0.5 and 0.8 in the ***v*** direction and 0.1 and 0.7 in the ***u*** direction (Figures 11b and 11d), and surface currents generally led Zi_{12} by 0–3 h (Figures 11a and 11c).

Over the DCH region, there is a ***u*** direction (***v*** direction) progressive time lag difference of 2–3 h from northwest to southeast (northeast to southwest) which is indicative of diurnal oscillation propagation (Figures 11a and 11c). The northeast and southeast corners of the domain exhibit sharp decreases in ***u*** direction correlations but not in the ***v*** direction.

Over the MBS, normalized correlations decreased to approximately 0.5 along the western edge of the HF radar domain (Figures 11c and 11d), and there is a ***u*** direction (***v*** direction) progressive time lag difference from the northwest corner of the MBS to the southeast (west to east) which is indicative of northwest to southeast propagation (Figures 11a and 11d).

Cross-correlation analyses performed over three 10 day sections of time similar to Figure 11 (not shown) captured the temporal evolution of the correlations. The reduced record length of the sections of time compromised confidence limits due to a decrease in the number of observed diurnal oscillations which reduce degrees of freedom (the 10% level of confidence was 0.5). Nonetheless, 10 day cross correlations between Zi_{12} and Zi_{40} with HF radar observations provided valuable insight. For approximately the first 10 days of the month, only *Zi*12 was well correlated with observations where normalized correlations were above 0.7 over much of the domain and time lags ranged between 0 and $^{+}3$ h. For the second 10 days, both *Zi*12 and *Zi*40 were well correlated (mostly above 0.7) and time lags for Zi_{12} ranged between $^{-}1$ and $^{+}1$ while time lags for Zi_{40} ranged between $^{+}2$ and $^{+}4$. For the last 10 days, *Zi*40 correlations were significant over most of the

Table 1. Linear Regression Results for Zi_{12} Versus HF Radar at Pt. A and Pt. B for June 2010

	R^2	Slope	*p* Value
pt. A			
u direction	0.25	0.50	5.25×10^{-46}
v direction	0.29	0.54	7.92×10^{-53}
pt. B			
u direction	0.38	0.79	4.78×10^{-73}
v direction	0.60	0.88	1.64×10^{-130}

Table 2. Linear Regression Results for Zi_{40} Versus HF Radar at Pt. A and Pt. B for June 2010

	R^2	Slope	p Value
pt. A			
u direction	0.12	0.37	6.84×10^{-22}
v direction	0.15	0.41	5.42×10^{-27}
pt. B			
u direction	0.03	0.26	1.38×10^{-6}
v direction	0.05	0.27	1.83×10^{-9}

MBS (0.5–0.6, time lags of $0–^{+}2$ h) but not over the DCH. In contrast, $Zi12$ correlations were good over most of the DCH (0.6–0.8, time lags of $^{+}2–^{+}4$ h) and diminished over the MBS.

3.6. Diurnal Complex Demodulation of *Zi* and HF Radar Measured Surface Currents

Complex demodulation has been used to successfully identify and describe near-inertial motions in previous studies including *Jarosz et al*. [2007], *Perkins* [1976], and *Simpson et al*. [2002]. The method is well described in *Emery and Thomson* [2001] and is applied by performing a least squares fit between observed current vectors in complex form as a function of time, $u(t) + iv(t)$, and a fabricated fixed amplitude vector in complex form rotating CCW and CW in time ($A\,exp(i\omega t)$ and $A\,exp(-i\omega t)$) where A is the amplitude of the vector and ω is the frequency. The results return a phase and amplitude where the phase represents the phase difference between the two signals and the amplitude is used to determine when the phase is valid. By performing complex demodulation analysis on intervals of time along a complex vector time series, a record of the evolving phase difference can be used to determine the evolving frequency of the time series oscillations in relation to ω. A negative (positive) temporal trend in the phase implies an observed signal frequency greater (less) than ω. We performed diurnal complex demodulation on overlapping 24 h sections of observed HF radar currents every 12 h with a fixed amplitude vector that rotated diurnally ($\omega = f_d = 24^{-1}$ h^{-1}). A minimum threshold of 10 cm/s in the amplitude is arbitrarily used to determine when the phase is valid. Because the diurnal oscillations in the NeGoM are predominantly CW, CCW complex demodulation results are insignificant and therefore not reported.

June 2010 diurnal complex demodulation applied to Zi_{40} does not exhibit notable trends in the overall phase slope when amplitudes were significant indicating that the Zi_{40} frequency is nearly diurnal (Figures 12a and 12b). This was particularly true after 9 June. Note that abrupt phase shifts typically occurred when amplitudes decreased below the 10 cm/s threshold which is to be expected. Diurnal complex demodulation applied to Zi_{12} shows that the Zi_{12} frequency is also nearly diurnal for the first 8 days of the month, but a negative phase slope thereafter indicates that the frequency became shifted slightly higher than f_d. The shifts toward higher frequencies for Zi_{12} are surprising for three reasons: (1) the local inertial frequency (f)

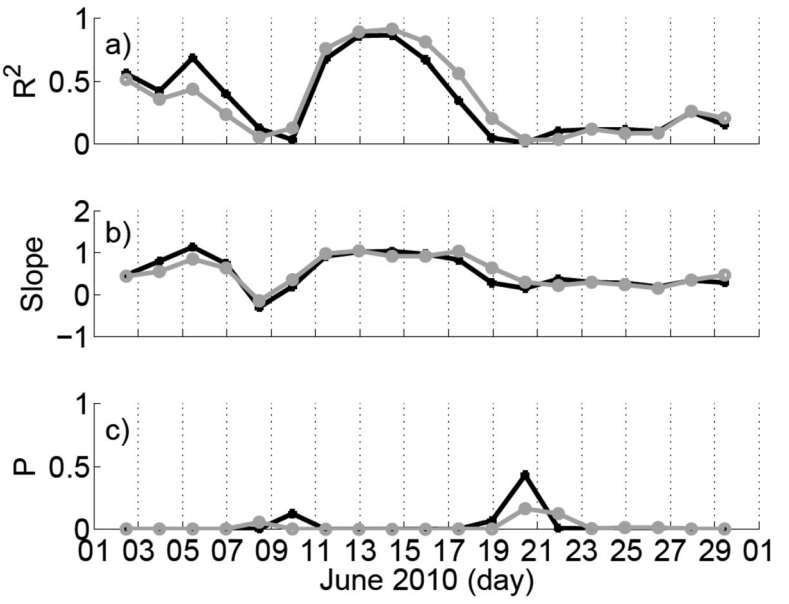

Figure 9. June 2010 running linear regression results comparing pt. A HF radar surface currents and Zi_{12}: (a) normalized R^2, (b) slope, and (c) p value. Black lines are for u direction and gray lines are for v direction. Overlapping 3 day linear regressions were performed every 1.5 days. This figure corresponds with Figure 3a.

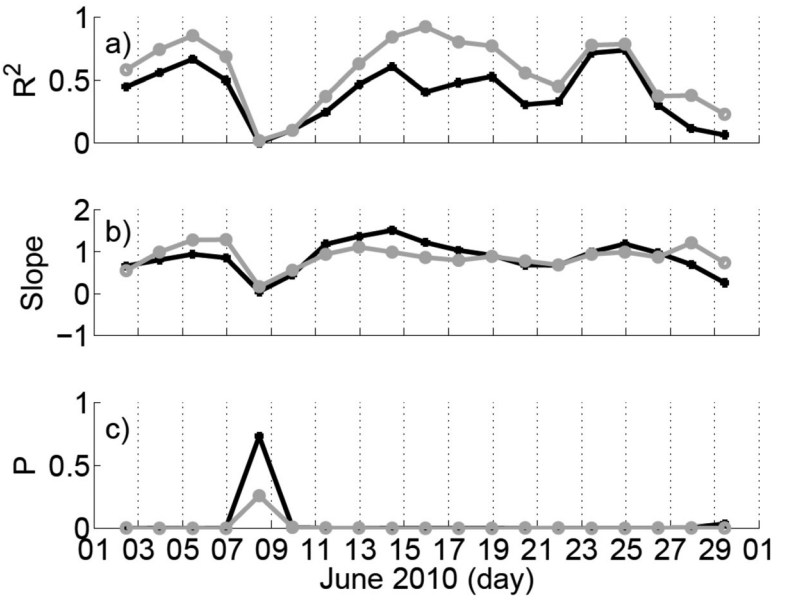

Figure 10. June 2010 running linear regression results comparing pt. A HF radar surface currents and Zi_{40}: (a) normalized R^2, (b) slope, and (c) *p* value. Black lines are for *u* direction and gray lines are for *v* direction. Overlapping 3 day linear regressions were performed every 1.5 days. This figure corresponds with Figure 4a.

used in the Zi_{12} calculation is very nearly diurnal, (2) there is no significant wind stress energy peak in the rotary spectra slightly higher than f_d (Figure 3b), and (3) *Pollard and Millard* [1970] state that the *Zi* frequency response should be slightly lower than *f* when the forcing frequency spectra is flat. Note, however, that there is a small energy peak slightly higher than f_d at buoy 42012 (Figure 3b). As observed, the Zi_{40} frequency response is expected to be lower than Zi_{12} due to the latitudinal difference between the two buoys, but like Zi_{12}, it is higher than expected.

The temporal frequency variability in the HF radar surface current oscillations at points A and B generally mirrored that of Zi_{12} which is supported by their respective phase changes in Figure 12. The negative phase slope for both Zi_{12} and observed oscillations after 10 June is estimated to be −15°/d which translates to a frequency of 1.043 cpd (or a 4% superinertial frequency shift from f_d). The superinertial shift in the surface currents is corroborated by energy at frequencies slightly greater than f_d in surface current rotary spectra

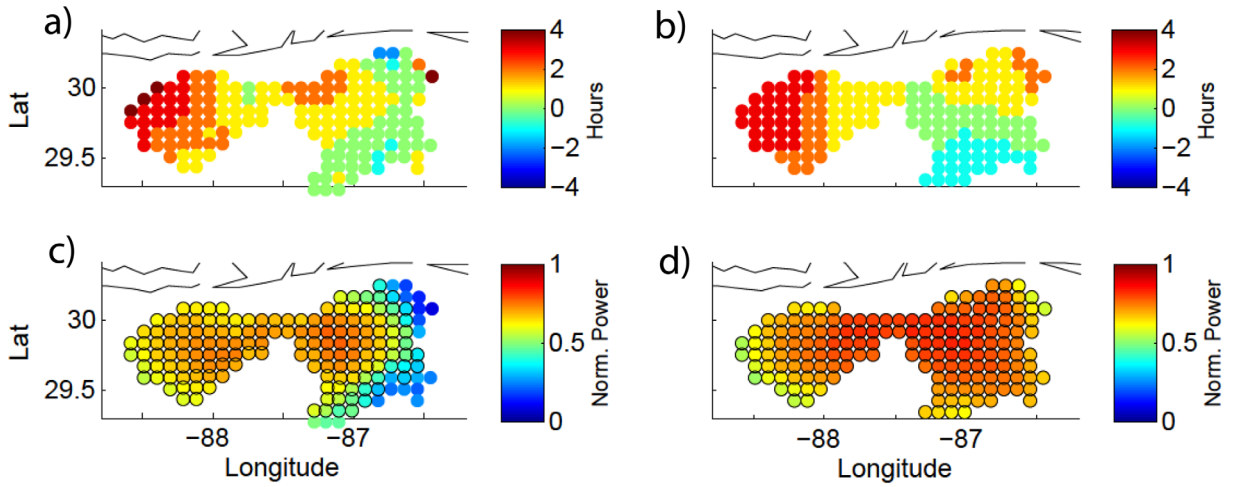

Figure 11. June 2010 cross correlation between Zi_{12} and HF radar surface currents. Time lag in (a) ***u*** direction and (b) ***v*** direction. Normalized correlation in (c) ***u*** direction and (d) ***v*** direction. Black circles indicate data points above the 10% level of significance which is 0.3 based on 31 degrees of freedom. Positive (negative) time lags indicate that the surface current oscillations lead (follow) the Zi_{12} oscillations.

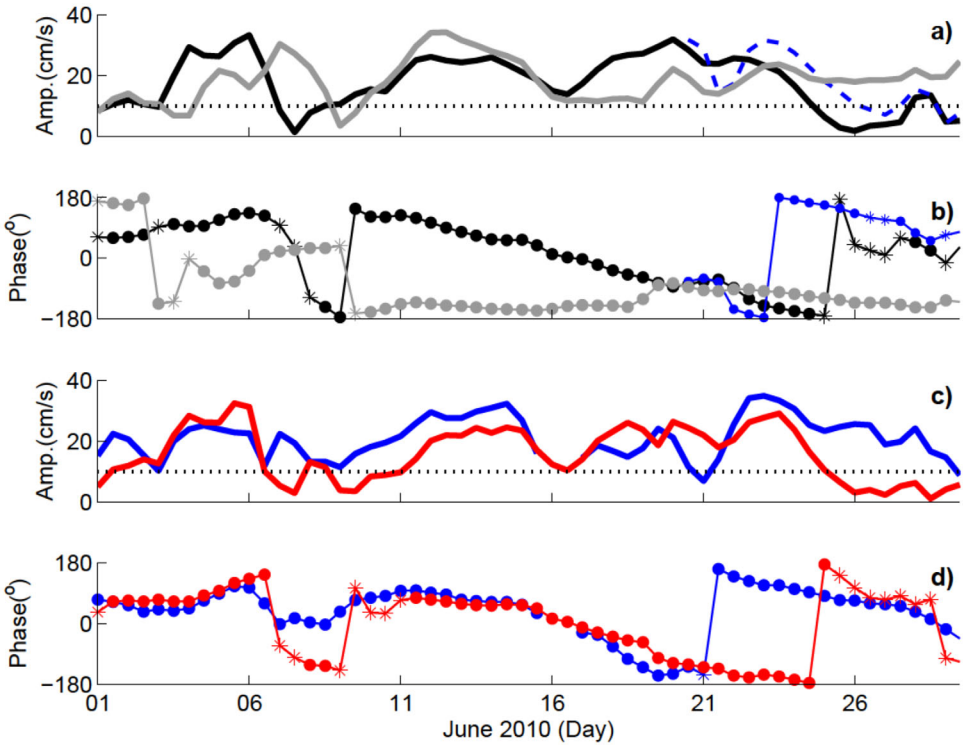

Figure 12. June 2010 CW diurnal complex demodulation (a) amplitude and (b) phase for Zi_{12} (black) and Zi_{40} (gray). CW diurnal complex demodulation (c) amplitude and (d) phase for surface current oscillations at HF radar data locations A (blue) and B (red).The blue lines and markers in Figures 12a and 12b are for the Zi_{12} calculation restarted on 20 June. The thin black dotted lines in Figures 12a and 12c indicate the 10 cm/s amplitude threshold. The stars in Figures 12b and 12d indicate phase when the amplitude decreased below the 10 cm/s threshold.

(Figures 3a and 3b). An observed global superinertial frequency shift from the local *f* in inertial oscillations is well documented and attributed to the dispersive properties of freely propagating internal-inertial waves on a β-plane [*Elipot and Lumpkin*, 2008; *Elipot et al*., 2010; *Fu*, 1981; *Garrett*, 2001]. *Elipot et al*. [2010] observed a 2.5% superinertial shift between 30°N(S) and the equator which was speculated to be due to the β-effect of internal-inertial waves constrained to equatorward propagation. They noted, however, that they were unable to discount the influence of local atmospheric forcing. The simultaneous superinertial shift in Zi_{12} and surface oscillations after 10 June, along with the overall superinertial shift from *f* in Zi_{12} and Zi_{40}, suggests that wind forcing is contributing to the superinertial shift in the surface oscillations at this time in the NeGoM.

Because the June 2010 superinertial shift in Zi_{12} was unexpected, diurnal complex demodulation on *Zi* was extended to include May–August 2010 (not shown). The frequencies of *Zi*, particularly Zi_{12}, were found not to be fixed and exhibit periods of diurnal frequency response along with periods of superinertial shifts as observed in June 2010. This shows that, as expected, there is a propensity for wind forcing and the inertial response to wind forcing at the critical latitude to exhibit an energy peak at f_d which is in agreement with *Jarosz et al*. [2007], but there is also a tendency for the oscillations to be shifted toward higher frequencies.

4. Discussion

4.1. Determination of Wind-Forced Inertial Oscillations

The ubiquitous summertime near-diurnal oscillations in the NeGoM must first be determined to be predominantly due to the inertial response to wind forcing, rather than diurnal tidal forcing, before further investigation. This is performed through the following series of comparative analyses between observed HF radar surface currents, *Zi*, and OTIS tidal current predictions: objective time series comparisons, linear regression analyses, spatial cross-correlation analyses, and complex demodulation analyses. The analyses presented in sections 2 and 3 are necessary because the inertial, tidal, and wind forcing frequencies are all nearly diurnal.

Harmonic analyses alone cannot resolve such small frequency differences unless considerably longer time series are used. In addition, the OTIS predicted spring tide and the calculated *Zi* oscillations frequently align with the observed HF radar surface current oscillations, and as previously mentioned, a higher-resolution tidal model may be required to resolve the tidal currents. If OTIS and the results from previous tidal model studies are correct [*Gouillon et al*., 2010; *He and Weisberg*, 2002a], then the barotropic tidal current amplitudes over the MBS (typically less than 12 cm/s) are relatively small compared to the surface current diurnal oscillations during the summer months. There are a numerous causes that can shift the phase or frequency of inertial oscillations and thus produce discrepancies between *Zi* and observed oscillations: errors in wind stress calculations due to highly variable winds and atmospheric stratification, local wind forcing recorded at the buoy from thunderstorms or wind-shifts along atmospheric fronts that are not representative of wind forcing over the domain, HF radar error, phase shifts due to barotropic and baroclinic tidal forcing, frequency shifts due to relative vorticity and advective Doppler shift [*Kunze*, 1985; *Mooers*, 1975; *Perkins*, 1972; *Pollard and Millard*, 1970; *White*, 1972], the tendency for *Zi* to predict a frequency less than *f* while the true ocean response is influenced by the Brunt-Väisälä frequency which shifts the frequency higher than *f* [*Pollard and Millard*, 1970], near-diurnal Helmholtz resonance [*Platzman*, 1972; *Reid et al*., 1981], internal waves generated at the coastline [*Millot and Crépon*, 1981], and a positive frequency shift due to the dispersive properties of freely propagating near-inertial waves.

Subjective visual comparisons of time series reveal some of the subtle similarities between *Zi* and surface current variability that are difficult to assess with objective methods. Overall, June 2010 *Zi* oscillatory time series variability compared favorably to HF radar data while OTIS tidal predictions drift in and out of phase and underpredict the amplitudes (Figures 7 and 8). Oscillation matches between Zi_{12} and HF radar were better at pt. B than at pt. A (Figure 7), which is reflected in linear regression fits in Table 1. Minor discrepancies with Zi_{12} at pt. A in June 2010 occurred between days 17 and 21 and continued to the end of the month when Zi_{12} oscillations decreased, which is reflected in the running linear regression analysis (Figure 9). The decrease in the Zi_{12} oscillation amplitudes between 7–11 and 25–28 June matched the decrease observed over the DCH region at pt. B, particularly the ***v*** component (Figure 7b). The surface oscillation linear regression results at pt. A for Zi_{12} and Zi_{40} (Tables 1 and 2) are not as high as expected due to the combined influence of wind forcing at the two buoys such that occasionally Zi_{12} better represented the oscillations over the MBS while at other times Zi_{40} better represented the oscillations. This can be seen in time series comparisons and running linear regression comparisons where Zi_{12} matches HF radar oscillations at the beginning of the month (Figures 7a and 9) and Zi_{40} matches HF radar oscillations near the end of the month (Figures 8 and 10).

Normalized cross correlations between Zi_{12} and HF radar surface currents were good, ranging between 0.6 and 0.8 over most of the domain with some exceptions (Figures 11c and 11d). By comparison, correlations with OTIS tidal predictions were relatively poor, ranging between 0.1 and 0.6 (not pictured).

The diurnal complex demodulation phase changes of HF radar surface currents and Zi_{12} are small at the beginning of June 2010 and simultaneously decrease at approximately $-15°$/d after 8 June (Figures 12a and 12c). The timing and magnitude of the negative phase slope in both Zi_{12} and surface currents indicate that the frequency shift is largely due to the inertial response to wind forcing rather than the numerous other mechanisms that can shift the frequency. In contrast, diurnal complex demodulation phase change of the predicted tides (not shown) increases with time since the resulting tidal frequency of the K_1 and O_1 interference is slightly less than diurnal. The phase change of Zi_{12} after 8 June is relatively constant in comparison to the phase changes observed in the HF radar oscillations. These discrepancies are likely due to the numerous other mechanisms that can shift the frequency of inertial oscillations.

Due to a much deeper forced layer, winter wind-driven inertial oscillation magnitudes are expected to be smaller than those during the summer. With the influence of wind-driven oscillations diminished, insight into how well OTIS is predicting the tides is possible. January 2011 HF radar ***v*** component surface current time series at pt. A compare favorably to OTIS tidal current predictions (Figure 13) and linear regression results returned $R^2 = 0.37$ and slope = 0.27. The oscillations are smaller than those observed during the summer and match the spring-neap cycle from O_1 and K_1 tidal interference. The reasoning here is that if OTIS is accurately predicting the amplitudes of the barotropic tidal currents during the winter when there is little influence from wind-driven inertial oscillations, then we can have greater confidence in the OTIS tidal predictions during June 2010. The observed ***u*** component oscillation amplitudes exhibited greater

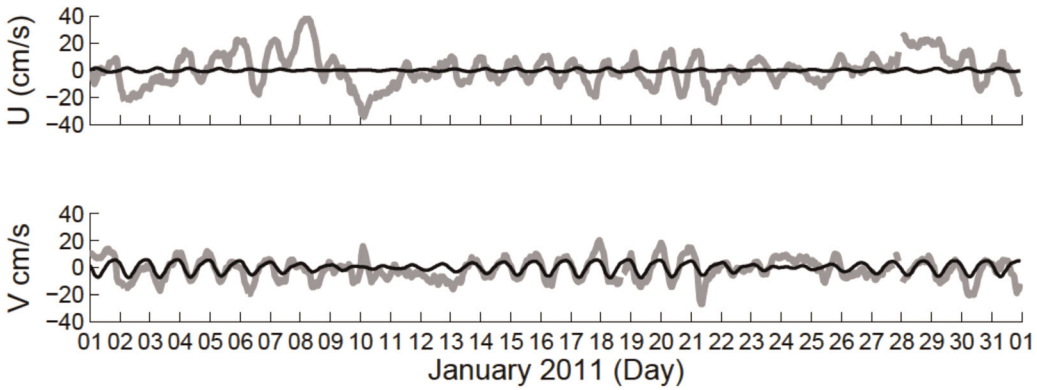

Figure 13. January 2011 (top) ***u*** and (bottom) ***v*** HF radar measured surface currents time series at pt. A (gray lines) and OTIS tidal prediction (black lines).

variability and did not match the small ***u*** component tidal currents predicted by OTIS. It is not clear why OTIS underpredicts the ***u*** component amplitudes. January 2011 spatial plots of the diurnal band percent total variance (not shown) exhibited the expected spatial tidal influence predicted by OTIS and previous modeling efforts [*Gouillon et al*., 2010; *He and Weisberg*, 2002a] where ***v*** component diurnal band variance increases over the MBS west of 87.75°W.

4.2. Spatiotemporal Variability of Inertial Oscillations

There is little evidence from the June 2010 HF radar data of the sharp increase in CW diurnal band variance over the slope south of the MBS observed by *Jarosz et al*. [2007]. Due to drop-offs in HF radar coverage, diurnal band variance is not investigated in this region. However, with diurnal band variance over the MBS reaching 80% (Figure 2) it is unlikely that there would be a significant increase in variance over the slope. The sharp CW variance gradient south of the MBS observed by *Jarosz et al*. [2007] occurred at about 29.2°N. In this region, enhanced oscillations south of 29.5°N on 11–16 June and at 29.2°N where oscillation amplitudes decreased to the north and south on 21–29 June can be observed in Figure 5c. The enhanced oscillations on 11–16 June may simply be due to strong eastward flow coupled with the Coriolis response which does not necessarily imply an increase indiurnal band variance. The enhanced oscillations on 21–29 June are in agreement with *Chen et al*. [1996] who observed an inertial oscillation maximum at the Texas-Louisiana shelf break with decreases to the north and south. Over the DCH, the gradual offshore and onshore decrease in diurnal band variance from the 100–200 m isobaths (Figure 2) is also in agreement with *Chen et al*. [1996], and in disagreement with *Jarosz et al*. [2007] who observed a gradual offshore increase in CW variance from the 200 m isobath. There are a number of reasons why our observations disagree with *Jarosz et al*. [2007]. Our analysis time interval is shorter, and there are occasional HF radar coverage drop-offs over the southern edge of the MBS. Strong shear at the bottom of the pycnocline generated by inertial oscillations could be responsible for discrepancies between HF radar observations, which measured the top 2.5 m of the water column, and the ADCPs used by *Jarosz et al*. [2007], which measured currents below 8–18 m. These ADCP measurements did not include most of the surface forced layer which is typically 8–10 m during the summer. Additionally, interannual or seasonal variability in the spatial extent of semifreshwater discharge can influence the depth of the forced layer and subsequently influence spatial variability of the inertial oscillations.

Propagation of the diurnal-inertial oscillation signals can be identified by spatial changes in cross-correlation time lags, and by diurnal signal tilts in the Hövmöller diagrams. The cross-correlation time-lag analysis suggests that the ***u*** direction (***v*** direction) diurnal-inertial signal generally propagates from northwest to the southeast (west to east) over the MBS, and from northwest to southeast (northeast to southwest) over the DCH (Figures 11a and 11b). The propagation speeds of the diurnal-inertial signals are roughly estimated to range between 3 and 8 m/s from the cross-correlation analyses. Propagation speeds were estimated to be 0–15 cm/s from the Hövmöller diagrams (Figures 4–6). Propagation directions from these diagrams generally agreed with propagation directions in the cross-correlation analyses. Over the DCH region, there is diurnal-inertial signal offshore propagation from the 100 m isobath between 11 and 20

June, which is connected to the enhanced inertial oscillations north of 30°N (Figure 6). There is also an abrupt decrease in the offshore propagation speed at the 100 m isobath (at approximately 29.5°N) south of the MBS between 22 and 30 June (Figure 5) which is associated with an abrupt phase change in the oscillations. Changes in the characteristics of the inertial motions along the 100 m isobath could be due to spatial stratification variability along with vorticity and/or Doppler-shift effects associated with strong eastward jet-like flow along the MBS break that gradually weakens and fans out over the DCH. The diurnal signal propagation implies Poincaré wave propagation where they are allowed to propagate freely south of 30°N [*Zhang et al*., 2010] but it can also imply spatial variability in the inertial response to wind forcing.

The enhanced diurnal inertial oscillations (amplitudes $\approx$ 50 cm/s) north of 30°N at the DCH are predominantly rectilinear, oriented across shore (Figure 6), and aligned with the mean onshore transport in this region (Figure 2). The enhanced amplitudes could be due to trapping of Poincaré waves north of 30°N [*Zhang et al*., 2010], or trapping due to negative vorticity [*Kunze*, 1985] associated with inner-shelf alongshore flow. Both of these processes can potentially enhance vertical mixing in the region. They are likely not tidal as the spring-neap cycle of K_1-O_1 interference is not observed, tidal currents are expected to be small [*He and Weisberg*, 2002a], and ***v*** component correlations with *Zi* are good (Figures 7b and 12 and Table 1).

Inertial oscillations over the MBS occasionally migrate out of phase with those over the DCH. This occurs on 12–16 June where there is an abrupt zonal shift in oscillations that occurs at approximately 87.5°W (Figure 4a, Box A), and on 22–30 June where there is a more gradual shift in the oscillations (Figure 4, Box B). The processes responsible for the two cases are different. The former case is due to a discontinuity in the west-east diurnal signal propagation. Zi_{12} and Zi_{40} are in phase at this time (Figures 7 and 8) which suggests homogeneous wind forcing over the domain. The latter case is more likely due to spatiotemporal variability in wind forcing and consequentially the inertial response. On 22–30 June, Zi_{12} and Zi_{40} are out of phase (Figures 7 and 8). Not only are Zi_{12} and Zi_{40} out of phase at this time, but Zi_{40} better describes the oscillations over the MBS (Figure 8) and Zi_{12} better describes the oscillations over the DCH (Figure 7b) as indicated by linear regression R^2 and slope values (Figures 9 and 10). Another influence on such abrupt inertial oscillation spatiotemporal variability could be due to spatial differences in stratification as the MBS is closer to larger sources of semifreshwater discharge. Abrupt changes in inertial oscillation variability can initiate vertical motions due to surface divergence and convergence which can enhance vertical mixing [*Hyder et al*., 2011]. Based on the above observations, this type of enhanced vertical mixing in June 2010 most likely occurred near 87.5°W, which roughly separates the MBS and DCH regions. The previously mentioned abrupt phase change at the southern edge of the MBS between 22 and 30 June (Figure 5) is another region where this type of mixing occurred.

Periods of ***u*** component oscillation suppression over the northern DCH, while ***v*** component oscillations are not suppressed, suggests some other type of mechanism related to the inertial response to wind forcing. These nearly rectilinear oscillations can be seen between 10 and 20 June at pt. B (Figure 7b), in the Hövmöller diagrams from 9 to 14 and 26 to 30 June (Figure 6a), and are reflected in the ***u*** component correlation decrease along the eastern region of the domain (Figure 11c). The oscillations are likely not tidal because ***v*** component Zi_{12} oscillations clearly match observed oscillations (Figure 7b, bottom). However, the suppressed ***u*** component of the oscillations is not expected for inertial motions (or Poincaré waves). Poincaré waves exhibit eccentric surface current vector ellipses with major/minor axes represented by ω/f where $\omega \geq f$. In this case, the episodic rectilinear oscillations were diurnal such that the major axes were represented by *f*. This would imply that $\omega < f$ which is not supported by the dispersion relationship for Poincaré waves. It is not known what is causing the ***u*** direction suppression of the oscillations although it could be related to internal waves generated by inertial motions impacting the coastline.

5. Summary and Concluding Remarks

We have demonstrated that the ubiquitous summer (June 2010) near-diurnal oscillations observed in the NeGoM are predominantly due to the inertial response to wind forcing and not due to diurnal tidal currents. The distinction between these two processes is important because they vertically mix the water column very differently. The unusually large inertial oscillations are due to resonance at the critical latitude for inertial motions in combination with a shallow forced layer associated with strong stratification. During the

winter (January 2011), presumably when there is a deep mixed layer, the near-diurnal oscillations are more likely to be attributed to tidal forcing, particularly over the MBS. Additionally, we have presented a unique spatiotemporal view of the wind-driven inertial currents which are used to identify regions of potential mixing enhancement in the NeGoM. Three regions in the NeGoM were identified where oil from the Deepwater Horizon spill was potentially subjected to vertical mixing by inertial motions: North of 30°N at the DCH, along 87.5°W, and along the southern edge of the MBS at 29.7°N.

The inertial oscillations were large in comparison with mean flow and exhibited considerable spatiotemporal variability. The observed oscillation frequency was essentially diurnal for the first 10 days of June 2010 before shifting to approximately 1.043 cpd, thereafter. The shift was attributed, in part, to a shift in the inertial response to wind forcing.

The MBS is characterized by large inertial motions, very little mean flow over the middle of the shelf, and high percent of total variance in the diurnal-inertial frequency band. Diurnal band variance ellipses are circular indicating that the oscillations are almost purely inertial. Some of the strongest diurnal oscillations occurred at the southern region of the MBS reaching amplitudes of 80 cm/s. The diurnal signal of the oscillations generally propagated from west to east.

Over the DCH, there is a gradual decrease in diurnal band variance toward the north and south from the 100–200 m isobath region. The oscillations generally propagated southward. Periods of north-south oriented rectilinear oscillations were observed over the northern extent of the DCH where mean flow was northward.

Although the diurnal oscillations were found to be predominantly due to the inertial response to wind forcing, there are discrepancies. Changes in inertial motion characteristics, particularly where there is west-east flow along the 100 m isobath coupled with strong stratification, suggest that this region is well suited for investigating the effects of vorticity, Doppler shift, and stratification on inertial waves. Another likely candidate for additional diurnal current variability is internal tides due to typically strong stratification in combination with a wide range of continental slope angles. Tidal focusing in the DeSoto Canyon and Sverdrup wave propagation over the MBS are also likely candidates. This illustrates the need for a comprehensive tidal model study in the region that can resolve the complex bathymetry and the strongly stratified shallow pycnocline.

Acknowledgments

This project was funded by the Consortium for Advanced Research on Transport of Hydrocarbon in the Environment (CARTHE) through the Gulf of Mexico Research Initiative (GoMRI), and was inspired by observations made during the CARTHE Grand Lagrangian Deployment (GLAD). We would like to thank the reviewers for their time, thoughtful suggestions, and contributions to this manuscript. Stephan Howden, Jamie Davis, and the rest of the HF radar team at University of Southern Mississippi maintain the radars, and provided the HF radar data. The HF radar data, GLAD shipboard ADCP data, and CTD data are available on the Gulf of Mexico Research Initiative Information and Data Cooperative (GRIIDC) website: (1) Surface Current Data from USM CODAR High Frequency Radar (doi:10.7266/N7KP803Z, udi:R1.x134.073:0036), (2) CARTHE: GLAD experiment near surface along-track ADCP measurements, northern Gulf of Mexico, July–August 2012 (doi:10.7266/N7TX3C9W), and (3) CARTHE: GLAD experiment CTD casts, northern Gulf of Mexico near DeSoto

References

Ardhuin, F., L. Marie, N. Rascle, P. Forget, and A. Roland (2009), Observation and estimation of Lagrangian, Stokes, and Eulerian currents induced by wind and waves at the sea surface, *J. Phys. Oceanogr.*, *39*(11), 2820–2838, doi:10.1175/2009jpo4169.1.

Barrick, D. (1971), Dependence of second-order Doppler sidebands in HF sea echo upon sea state, paper presented at Antennas and Propagation Society International Symposium, Sep., IEEE, Los Angeles, Calif.

Barrick, D. (1972), First-order theory and analysis of MF/HF/VHF scatter from the sea, *IEEE Trans. Antennas Propag.*, *20*(1), 2–10, doi:10.1109/TAP.1972.1140123.

Barrick, D., and B. Lipa (1979), A compact transportable HF radar system for directional coastal wave field measurements, in *Ocean Wave Climate*, edited by M. Earle and A. Malahoff, pp. 153–201, Springer US, N. Y., doi:10.1007/978-1-4684-3399-9_7.

Carter, G. S. (2010), Barotropic and baroclinic M2 tides in the Monterey Bay region, *J. Phys. Oceanogr.*, *40*(8), 1766–1783, doi:10.1175/2010JPO4274.1.

Chapman, R. D., and H. C. Graber (1997), Validation of HF radar measurements, *Oceanography*, *10*(2), 76–79, doi:10.5670/oceanog.1997.28.

Chapman, R. D., L. K. Shay, H. C. Graber, J. B. Edson, A. Karachintsev, C. L. Trump, and D. B. Ross (1997), On the accuracy of HF radar surface current measurements: Intercomparisons with ship-based sensors, *J. Geophys. Res.*, *102*(C8), 18,737–18,748, doi:10.1029/97JC00049.

Chen, C. S., and L. Xie (1997), A numerical study of wind-induced, near-inertial oscillations over the Texas-Louisiana shelf, *J. Geophys. Res.*, *102*(C7), 15,583–15,593, doi:10.1029/97JC00228.

Chen, C. S., R. O. Reid, and W. D. Nowlin (1996), Near-inertial oscillations over the Texas Louisiana shelf, *J. Geophys. Res.*, *101*(C2), 3509–3524, doi:10.1029/95JC03395.

Daddio, E., W. J. Wiseman, and S. P. Murray (1978), Inertial currents over the inner shelf near 30°N, *J. Phys. Oceanogr.*, *8*(4), 728–733, doi:10.1175/1520-0485(1978)008 < 0728:ICOTIS>2.0.CO;2.

D'Asaro, E. A. (1985), The energy flux from the wind to near-inertial motions in the surface mixed layer, *J. Phys. Oceanogr.*, *15*(8), 1043–1059.

D'Asaro, E. A., C. C. Eriksen, M. D. Levine, C. A. paulson, P. Niiler, and P. Van Meurs (1995), Upper-ocean inertial currents forced by a strong storm. Part I: Data and comparisons with linear theory, *J. Phys. Oceanogr.*, *25*(11), 2909–2936, doi:10.1175/1520-0485(1995)025 < 2909:UOICFB>2.0.CO;2.

Davies, A. M., and J. Xing (2003), On the interaction between internal tides and wind-induced near-inertial currents at the shelf edge, *J. Geophys. Res.*, *108*(C3), 3099, doi:10.1029/2002JC001375.

Dietrich, J. C., et al. (2012), Surface trajectories of oil transport along the Northern Coastline of the Gulf of Mexico, *Cont. Shelf Res.*, *41*, 17–47, doi:10.1016/j.csr.2012.03.015.

DiMarco, S. F., M. K. Howard, and R. O. Reid (2000), Seasonal variation of wind-driven diurnal current cycling on the Texas-Louisiana Continental Shelf, *Geophys. Res. Lett.*, *27*(7), 1017–1020, doi:10.1029/1999GL010491.

Canyon, July–August 2012 (doi:10.7266/N73X84KZ). Conversations with Timor Radko (Naval Postgraduate School) were helpful and insightful.

Dzwonkowski, B., and K. Park (2012), Subtidal circulation on the Alabama shelf during the Deepwater Horizon oil spill, *J. Geophys. Res.*, *117*, C03027, doi:10.1029/2011JC007664.

Ekman, V. W. (1905), On the influence of the earth's rotaion on ocean currents, *Ark. Mat. Astron. Fys.*, *2*(11), 1–53.

Elipot, S., and R. Lumpkin (2008), Spectral description of oceanic near-surface variability, *Geophys. Res. Lett.*, *35*, L05606, doi:10.1029/2007GL032874.

Elipot, S., R. Lumpkin, and G. Prieto (2010), Modification of inertial oscillations by the mesoscale eddy field, *J. Geophys. Res.*, *115*, C09010, doi:10.1029/2009JC005679.

Emery, W. J., and R. E. Thomson (2001), Chapter 5—Time-series analysis methods, in *Data Analysis Methods in Physical Oceanography*, edited by W. J. E. E. Thomson, pp. 371–567, Elsevier Sci., Amsterdam, doi:10.1016/B978-044450756-3/50006-X.

Fu, L. L. (1981), Observations and models of inertial waves in the deep ocean, *Rev. Geophys.*, *19*(1), 141–170.

Garrett, C. (2001), What is the "Near-Inertial" Band and Why Is It Different from the Rest of the Internal Wave Spectrum?, *J. Phys. Oceanogr.*, *31*(4), 962–971, doi:10.1175/1520-0485(2001)031 < 0962:WITNIB>2.0.CO;2.

Gonella, J. (1972), A rotary-component method for analysing meteorological and oceanographic vector time series, *Deep Sea Res. Oceanogr. Abstr.*, *19*(12), 833–846, doi:10.1016/0011-7471(72)90002-2.

Gouillon, F., S. L. Morey, D. S. Dukhovskoy, and J. J. O'Brien (2010), Forced tidal response in the Gulf of Mexico, *J. Geophys. Res.*, *115*, C10050, doi:10.1029/2010JC006122.

Hamilton, P., T. J. Berger, J. J. Singer, E. Waddell, J. H. Churchill, R. R. Leben, T. N. Lee, and W. Sturges (2000), *Desoto Canyon Eddy Intrusion Study: Final Report, vol. I, Executive Summary, OCS Study MMS 2000-079*, edited by Minerals Management Service, 37 pp., U.S. Dep. of the Inter., Gulf of Mex. OCS Reg., New Orleans, La.

He, R., and R. H. Weisberg (2002a), Tides on the West Florida Shelf, *J. Phys. Oceanogr.*, *32*(12), 3455–3473, doi:10.1175/1520-0485(2002)032 < 3455:TOTWFS>2.0.CO;2.

He, R., and R. H. Weisberg (2002b), West Florida shelf circulation and temperature budget for the 1999 spring transition, *Cont. Shelf Res.*, *22*(5), 719–748, doi:10.1016/S0278-4343(01)00085-1.

Hendershott, M. C. (1973), Inertial oscillations of tidal period, *Prog. Oceanogr.*, *6*, 1–27.

Hsueh, Y., and Y. Golubev (2001), A numerical model calculation of the flow in DeSoto Canyon in response to northerly wind bursts in winter, *Gulf Mex. Sci.*, *1*, 44–59.

Huh, O. K., W. J. Wiseman Jr., and L. J. Rouse Jr. (1981), Intrusion of loop current waters onto the west Florida continental shelf, *J. Geophys. Res.*, *86*(C5), 4186–4192, doi:10.1029/JC086iC05p04186.

Hyder, P., J. H. Simpson, J. Xing, and S. T. Gille (2011), Observations over an annual cycle and simulations of wind-forced oscillations near the critical latitude for diurnal–inertial resonance, *Cont. Shelf Res.*, *31*(15), 1576–1591, doi:10.1016/j.csr.2011.06.001.

Jarosz, E., Z. R. Hallock, and W. J. Teague (2007), Near-inertial currents in the DeSoto Canyon region, *Cont. Shelf Res.*, *27*(19), 2407–2426.

Kaplan, D. M., J. Largier, and L. W. Botsford (2005), HF radar observations of surface circulation off Bodega Bay (northern California, USA), *J. Geophys. Res.*, *110*, C10020, doi:10.1029/2005JC002959.

Kunze, E. (1985), Near-inertial wave propagation in geostrophic shear, *J. Phys. Oceanogr.*, *15*(5), 544–565, doi:10.1175/1520-0485(1985)015 < 0544:NIWPIG>2.0.CO;2.

Large, W. G., and S. Pond (1981), Open ocean momentum flux measurements in moderate to strong winds, *J. Phys. Oceanogr.*, *11*(3), 324–336, doi:10.1175/1520-0485(1981)011 < 0324:OOMFMI>2.0.CO;2.

Liu, Y., R. H. Weisberg, C. R. Merz, S. Lichtenwalner, and G. J. Kirkpatrick (2010), HF radar performance in a low-energy environment: CODAR SeaSonde Experience on the west Florida shelf*, *J. Atmos. Oceanic Technol.*, *27*(10), 1689–1710, doi:10.1175/2010JTECHO720.1.

Millot, C., and M. Crépon (1981), Inertial oscillations on the continental shelf of the Gulf of Lions—Observations and theory, *J. Phys. Oceanogr.*, *11*(5), 639–657, doi:10.1175/1520-0485(1981)011 < 0639:IOOTCS>2.0.CO;2.

Mooers, C. N. K. (1975), Several effects of a baroclinic current on the cross-stream propagation of inertial-internal waves, *Geophys. Fluid Dyn.*, *6*(3), 245–275, doi:10.1080/03091927509365797.

Morey, S. L., J. J. O'Brien, W. W. Schroeder, and J. Zavala-Hidalgo (2002), Seasonal variability of the export of river discharged freshwater in the northern Gulf of Mexico, paper presented at OCEANS '02 MTS/IEEE, MTS/IEEE, vol. 3, pp. 1480–1484, Biloxi, Miss., 29–31 Oct., doi:10.1109/OCEANS.2002.1191856.

Morey, S. L., W. W. Schroeder, J. J. O'Brien, and J. Zavala-Hidalgo (2003), The annual cycle of riverine influence in the eastern Gulf of Mexico basin, *Geophys. Res. Lett.*, *30*(16), 1867, doi:10.1029/2003GL017348.

Ohlmann, C., P. White, L. Washburn, B. Emery, E. Terrill, and M. Otero (2007), Interpretation of coastal HF radar–Derived surface currents with high-resolution drifter data, *J. Atmos. Oceanic Technol.*, *24*(4), 666–680, doi:10.1175/JTECH1998.1.

Paduan, J. D., and L. K. Rosenfeld (1996), Remotely sensed surface currents in Monterey Bay from shore-based HF radar (Coastal Ocean Dynamics Application Radar), *J. Geophys. Res.*, *101*(C9), 20,669–20,686, doi:10.1029/96JC01663.

Perkins, H. (1972), Inertial oscillations in the Mediterranean, *Deep Sea Res. Oceanogr. Abstr.*, *19*(4), 289–296, doi:10.1016/0011-7471(72)90022-8.

Perkins, H. (1976), Observed effect of an eddy on inertial oscillations, *Deep Sea Res. Oceanogr. Abstr.*, *23*(11), 1037–1042, doi:10.1016/0011-7471(76)90879-2.

Platzman, G. W. (1972), Two-dimensional free oscillations in natural basins, *J. Phys. Oceanogr.*, *2*(2), 117–138, doi:10.1175/1520-0485(1972)002 < 0117:TDFOIN>2.0.CO;2.

Poje, A. C., et al. (2014), Submesoscale dispersion in the vicinity of the Deepwater Horizon spill, *Proc. Natl. Acad. Sci. U. S. A.*, *111*(35), 12,693–12,698, doi:10.1073/pnas.1402452111.

Pollard, R. T. (1970), On the generation by winds of inertial waves in the ocean, *Deep Sea Res. Oceanogr. Abst.*, *17*(4), 795–812, doi:10.1016/0011-7471(70)90042-2.

Pollard, R. T., and R. C. Millard (1970), Comparison between observed and simulated wind-generated inertial oscillations, *Deep Sea Res. Oceanogr. Abstr.*, *17*(4), 813–821, doi:10.1016/0011-7471(70)90043-4.

Reid, J. L., Jr. (1962), Observations of inertial rotation and internal waves, *Deep Sea Res. Oceanogr. Abstr.*, *9*(7–10), 283–289, doi:10.1016/0011-7471(62)90011-6.

Reid, R. O., R. E. Whitaker, Texas A & M University, Department of Oceanography, and United States Army Engineer Waterways Experiment Station (1981), *Numerical Model for Astronomical Tides in the Gulf of Mexico*, Tex. A & M Univ., Dep. of Oceanogr., College Station.

Rotunno, R. (1983), On the linear theory of the land and sea breeze, *J. Atmos. Sci.*, *40*(8), 1999–2009, doi:10.1175/1520-0469(1983)040 < 1999:OTLTOT>2.0.CO;2.

Seim, H. E., B. Kjerfve, and J. E. Sneed (1987), Tides of Mississippi sound and the adjacent continental shelf, *Estuarine Coastal Shelf Sci.*, *25*, 143–156.

Simpson, J. H., P. Hyder, T. P. Rippeth, and I. M. Lucas (2002), Forced oscillations near the critical latitude for diurnal-inertial resonance, *J. Phys. Oceanogr.*, *32*(1), 177–187, doi:10.1175/1520-0485(2002)032 < 0177:FONTCL>2.0.CO;2.

Smith, S. R., and G. A. Jacobs (2005), Seasonal circulation fields in the northern Gulf of Mexico calculated by assimilating current meter, shipboard ADCP, and drifter data simultaneously with the shallow water equations, *Cont. Shelf Res.*, *25*(2), 157–183, doi:10.1016/j.csr.2004.09.010.

Stewart, R. H., and J. W. Joy (1974), HF radio measurements of surface currents, *Deep Sea Res. Oceanogr. Abstr.*, *21*(12), 1039–1049, doi:10.1016/0011-7471(74)90066-7.

Teague, W. J., H. W. Wijesekera, E. Jarosz, A. Lugo-Fernández, and Z. R. Hallock (2014), Wavelet analysis of near-inertial currents at the East Flower Garden Bank, *Cont. Shelf Res.*, *88*, 47–60, doi:10.1016/j.csr.2014.06.013.

Wang, D.-P., L.-Y. Oey, T. Ezer, and P. Hamilton (2003), Near-surface currents in DeSoto Canyon (1997â€''99): Comparison of current meters, satellite observation, and model simulation, *J. Phys. Oceanogr.*, *33*(1), 313–326, doi:10.1175/1520-0485(2003)033 < 0313:NSCIDC>2.0.CO;2.

Webster, F. (1968), Observations of inertial-period motions in the deep sea, *Rev. Geophys.*, *6*(4), 473–490, doi:10.1029/RG006i004p00473.

Weisberg, R. H., R. He, Y. Liu, and J. I. Virmani (2005), West Florida shelf circulation on synoptic, seasonal, and interannual time scales, in *Circulation in the Gulf of Mexico: Observations and Models*, edited by W. Sturges and A. Lugo-Fernandez, pp. 325–347, AGU, Washinton, D. C., doi:10.1029/161GM23.

White, W. B. (1972), Doppler shift in the frequency of inertial waves observed in moored spectra, *Deep Sea Res. Oceanogr. Abstr.*, *19*(8), 595–600, doi:10.1016/0011-7471(72)90042-3.

Whitt, D. B., and L. N. Thomas (2014), Resonant generation and energetics of wind-forced near-inertial motions in a geostrophic flow, *J. Phys. Oceanogr.*, *45*(1), 181–208, doi:10.1175/JPO-D-14-0168.1.

Yan, H., and R. A. Anthes (1987), The effect of latitude on the Sea Breeze, *Mon. Weather Rev.*, *115*(5), 936–956, doi:10.1175/1520-0493(1987)115 < 0936:TEOLOT>2.0.CO;2.

Yuan, D. (2002), A numerical study of barotropicly forced intrusion in DeSoto Canyon, *J. Geophys. Res.*, *107*(C2), 3010, doi:10.1029/2001JC000793.

Zhang, X., S. F. Dimarco, D. C. Smith Iv, M. K. Howard, A. E. Jochens, and R. D. Hetland (2009), Near-resonant ocean response to sea breeze on a stratified continental shelf, *J. Phys. Oceanogr.*, *39*(9), 2137–2155.

Zhang, X., D. C. Smith, S. F. DiMarco, and R. D. Hetland (2010), A numerical study of sea-breeze-driven ocean poincare wave propagation and mixing near the critical latitude, *J. Phys. Oceanogr.*, *40*(1), 48–66, doi:10.1175/2009JPO4216.1.